Journal of Nanobiotechnology

RESEARCH Open Access

Infection microenvironment-triggered nanoparticles eradicate MRSA by thermally amplified chemodynamic therapy and M1 macrophage

Qimin Hong[1†], Wei Zhang[1†], Zhen Liu[1†], Bo Li[2], Xi Liu[3], Zhinan Wang[3], Rui Wang[2], Jianping Yang[2*], Bin'en Nie[1*] and Bing Yue[1*]

Abstract

It is of great significance to develop a novel approach to treat bacterial infections, as the frequent misuse of antibiotics leads to the serious problem of bacterial resistance. This study proposed antibiotic-free antibacterial nanoparticles for eliminating methicillin-resistant *Staphylococcus aureus* (MRSA) based on a multi-model synergistic antibacterial ability of chemodynamic therapy (CDT), photothermal effect, and innate immunomodulation. Specifically, a polydopamine (PDA) layer coated and Ag nanoparticles loaded core-shell structure Fe_3O_4 nanoparticles (Fe_3O_4@PDA-Ag) is prepared. The Fe_3O_4 catalyzes H_2O_2 present in acidic microenvironment of bacterial infection into more toxic reactive oxygen species (ROS) and synergizes with the released Ag ions to exert a stronger bactericidal capacity, which can be augmented by photothermal action of PDA triggered by near-infrared light and loosen the biofilm by photothermal action to promote the penetration of ROS and Ag ion into the biofilm, result in disrupting biofilm structure along with killing encapsulated bacteria. Furthermore, Fe_3O_4@PDA-Ag exerts indirect antibacterial effects by promoting M1 macrophage polarizing. Animal models demonstrated that Fe_3O_4@PDA-Ag effectively controlled MRSA-induced infections through photothermal enhanced CDT, Ag^+ releasing, and macrophage-mediated bactericidal properties. The acid-triggered antibacterial nanoparticles are expected to combat drug-resistant bacteria infection.

Introduction

Bacterial antimicrobial resistance (AMR), is emerging as one of the greatest risks to global public health. [1] Drug-resistant bacterial infections currently kill at least 700,000 people worldwide each year, and predictably cause more than 10 million deaths annually by the year 2050, resulting in a cumulative cost to the global economy of approximately $100 trillion. [2, 3] This could be attributed to the increased and inappropriate use of antibiotics in medical practice, as well as the lack of stewardship and education on drugs. [4–7] On the other hand, biofilm formatted by bacteria against unfavorable factors effectively

†Qimin Hong, Wei Zhang and Zhen Liu contributed equally to this work.

*Correspondence:
Jianping Yang
jianpingyang@dhu.edu.cn
Bin'en Nie
niebinen2010@163.com
Bing Yue
advbmp2@163.com

Full list of author information is available at the end of the article

Graphical abstract

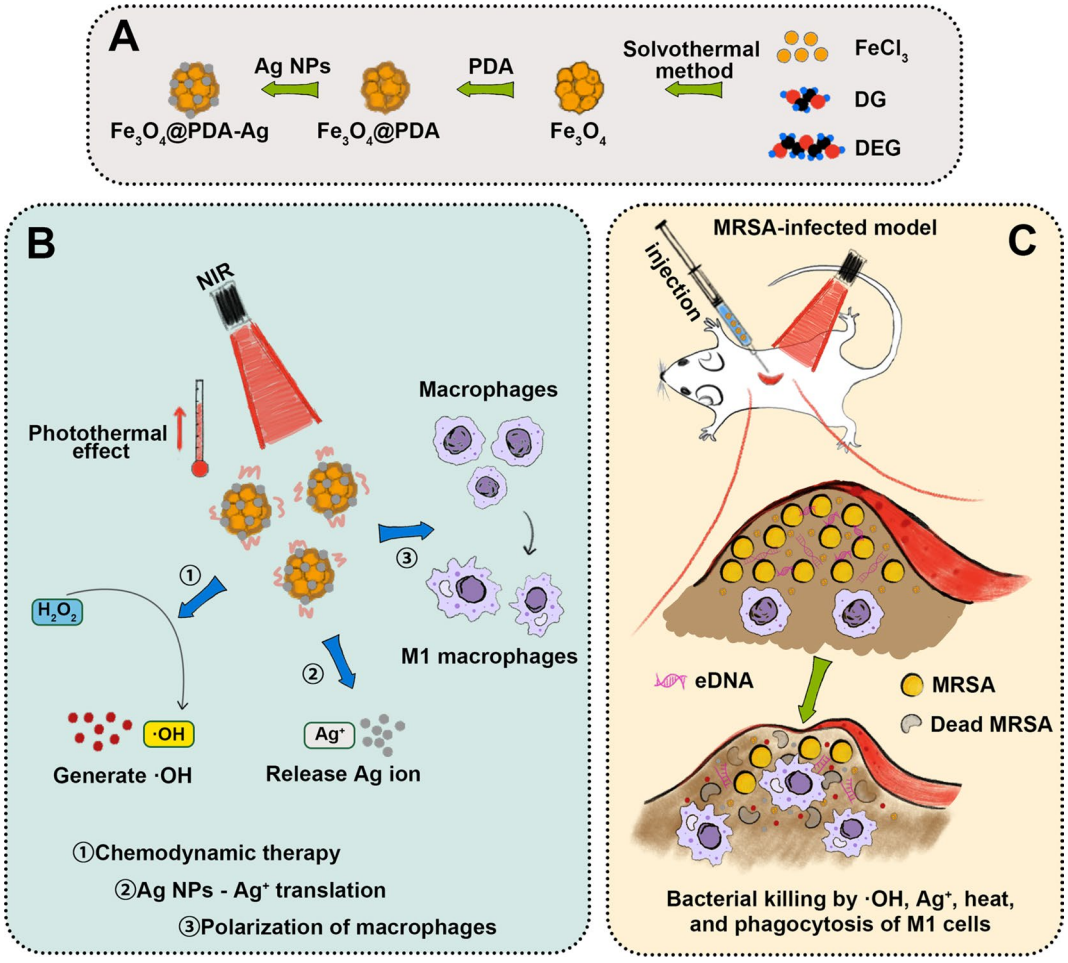

Keywords Nanoparticles, Synergistic antibacterial, Chemodynamic therapy, Photothermal, Macrophage

prevents the penetration of antibiotics and suppresses the host immune response, exacerbating the AMR situation. [8–10] Moreover, hypoxia, acidic extracellular pH, high H_2O_2 content and glutathione overexpression in the infection microenvironment (IME) represent another formidable challenge to eradicate antimicrobial resistance bacteria. [11, 12]

The speed of novel antibiotics far fails to keep up with bacterial resistance, with the risks of long times and high costs. [13, 14] Fortunately, nanotechnology-based material synthesis has opened unlimited possibilities for combating AMR, [15] as they have an intrinsic antimicrobial activity that the natural defense arsenal of bacteria may not hinder. [16] Compared to conventional antibiotics, these materials have immunomodulatory effects and interactions with host innate immunity that we have previously overlooked. [17–20] Among these, metallic nanomaterial has been explored for treating AMR infections due to their broader spectrum of antibacterial activity and lower bacterial resistance. [21–23] Silver nanoparticles are the most representative, which induces bacterial death by releasing reactive oxygen species (ROS) and Ag^+. [24, 25] In addition, the antimicrobial capacity that can be triggered/enhanced under specific conditions to reduce side effects is another huge advantage of nanomaterials. A variety of new antimicrobial modalities have been derived from this. In the case of chemodynamic therapy (CDT), for example, the iron-based nanomaterials trigger the Fenton reaction in IME, catalyzing endogenous H_2O_2 into cytotoxic hydroxyl radicals (·OH) to kill bacteria cells. [26, 27] Similarly, sonodynamic therapy (SDT) uses ultrasound to activate acoustic sensitizers to produce ROS, [28, 29] photodynamic therapy (PDT) uses laser-triggered photosensitizers to produce ROS, [30] and photothermal therapy (PTT) relies on the destruction of bacterial structures by the thermal effect triggered by

photothermal agents, [31, 32] all showing great potential in antimicrobial therapy without fear of resistance. Furthermore, combining the above monomodal antimicrobial modalities improves the antibacterial performance, showing the effect of "1+1>2" [33]. Take the combination of CDT and PTT for example: CDT produces ·OH that increases the sensitivity of bacterial cell membranes to heat, thereby reducing the dose of photothermal agent and laser intensity; while the temperature of PTT excitation, in addition to promoting CDT reaction, can also increase the permeability of pathogenic microbial cell membranes, thereby increasing the penetration rate of ROS [34]. The combination of Ag NPs and PTT also has a synergistic antibacterial effect [35, 36]: PTT promotes the release of Ag^+ and the disruption of bacterial cell membranes, allowing more Ag^+ to enter the bacteria, thus reducing the dose of Ag NPs and ensuring safety.

Innate immunity serves a vital role in clearing the pathogen. However, in the context of immunity to bacterial infections, the role of the innate immune system in the immunotherapy of bacterial infections has long been neglected. It has been shown that S. aureus biofilm-associated monocytes can polarize to an anti-inflammatory phenotype, promoting biofilm formation and acting as an "accomplice" to biofilm formation [37, 38]; pro-inflammatory stimulation of intracellular energy metabolism from oxidative phosphorylation to glycolysis leads to macrophage activation and thus inhibits biofilm development, highlighting the key role of monocytes/macrophages in determining biofilm persistence [39]. This highlights the critical role of the inflammatory state of monocytes/macrophages in determining biofilm persistence. Among the major cellular players involved in MRSA control, macrophages are essential in recognizing and eliciting bacterial clearance [40]. In return, *Staphylococcus aureus* could keep its survival by regulating macrophage phenotype. The M2 macrophages promote the antibiotic tolerance of *Staphylococcus aureus* [41]. Macrophages have excellent plasticity and play an important role in the clearance of pathogens [42]. However, relying solely on increasing the body's active immunity to antimicrobials exerts limited antimicrobial effects, and when bacterial biofilms are formed, achieving antimicrobials by increasing the body's active immunity appears inefficient in terms of antimicrobial efficacy. At the same time, the excessive inflammatory response brought about by macrophage immune antimicrobials is also likely to inhibit wound healing. Therefore, active body immunity must be synergized with passive antimicrobial agents to exert early passive antimicrobial activity, enhance intrinsic immune antimicrobial activity, and improve bacterial clearance efficiency.

Thus, developing nanomaterials with high efficacy in eradicating bacteria while awakening the macrophages and restoring their instinctive killing role is urgently needed. In the present study, we proposed acid-triggered multimodal synergistic antimicrobial nanoparticles. Specifically, Fe_3O_4 nanoparticles were synthesized by a solvothermal method first, then a polydopamine (PDA) layer was coated on the surface to form Fe_3O_4@PDA (FP), following Ag nanoparticles (NPs) loading, resulting in Fe_3O_4@PDA-Ag (FPA). Under the acid infection environment, Fe_3O_4 catalyzes H_2O_2 into more toxic ROS, synergizing with the released Ag ions to exert a stronger bactericidal capacity, which the photothermal action of PDA can augment. In the presence of a biofilm, FPA that exerts a thermal effect promotes the penetration of ROS and Ag^+ into heat-induced loose biofilms, accelerating the destruction of biofilms and the death of encapsulated bacteria. We expect to achieve a non-antibiotic method to combat drug-resistant bacteria infections and delay the development of bacterial resistance.

Results and discussion

Synthesis and characterization of Ag nanoparticles loaded core-shell structure Fe_3O_4 nanoparticles

According to transmission electron microscopy (TEM) and scanning electron microscopy (SEM) results (Fig. 1A), Fe_3O_4 is a spherical particle with a rough surface, whereas Fe_3O_4@PDA has a typical core-shell structure with a smooth surface, Fe_3O_4 as the core and 8 nm thick PDA layer as the shell. Because of the high adhesion of PDA, partial bonding was observed between the particles. Globular Ag NPs approximately 50 nm in size were loaded onto the Fe_3O_4@PDA surface. The elemental composition of Fe_3O_4@PDA-Ag was determined using energy-dispersive spectrometry (EDS) with the mass ratio of Ag being approximately 32.15% (Figure S1). Size analysis of the nanoparticles (Fig. 1B) revealed a larger size than that observed by electron microscopy, which may be due to the hydrated layer caused by hydrophilic hydroxyl groups on the surfaces of the Fe_3O_4 and PDA layers. For Fe_3O_4@PDA-Ag, a small peak at approximately 60 nm was observed, which may be caused by the shedding of Ag NPs after sonication. The zeta potentials of each nanoparticle were −16.0 mV (Fe_3O_4), -33.3 mV (Fe_3O_4@PDA), and −30.9 mV (Fe_3O_4@PDA-Ag), respectively (Fig. 1C).

In the results of X-ray diffraction (XRD) (Figure S2A) of Fe_3O_4, the diffraction peaks of 2θ angles at 30.2°, 35.5°, 43.1°, 53.5°, 57.1°, and 62.6° were observed, corresponding to (220), (311), (400), (422), (511) and (440) of Fe_3O_4 crystal. The Fe_3O_4@PDA spectra are consistent with that of Fe_3O_4 owing to the amorphous structure of PDA. When the Ag NPs were loaded, a characteristic diffraction peak was observed at 38.3° corresponding to the (111) plane of Ag. In the X-ray photoelectron spectroscopy (XPS)

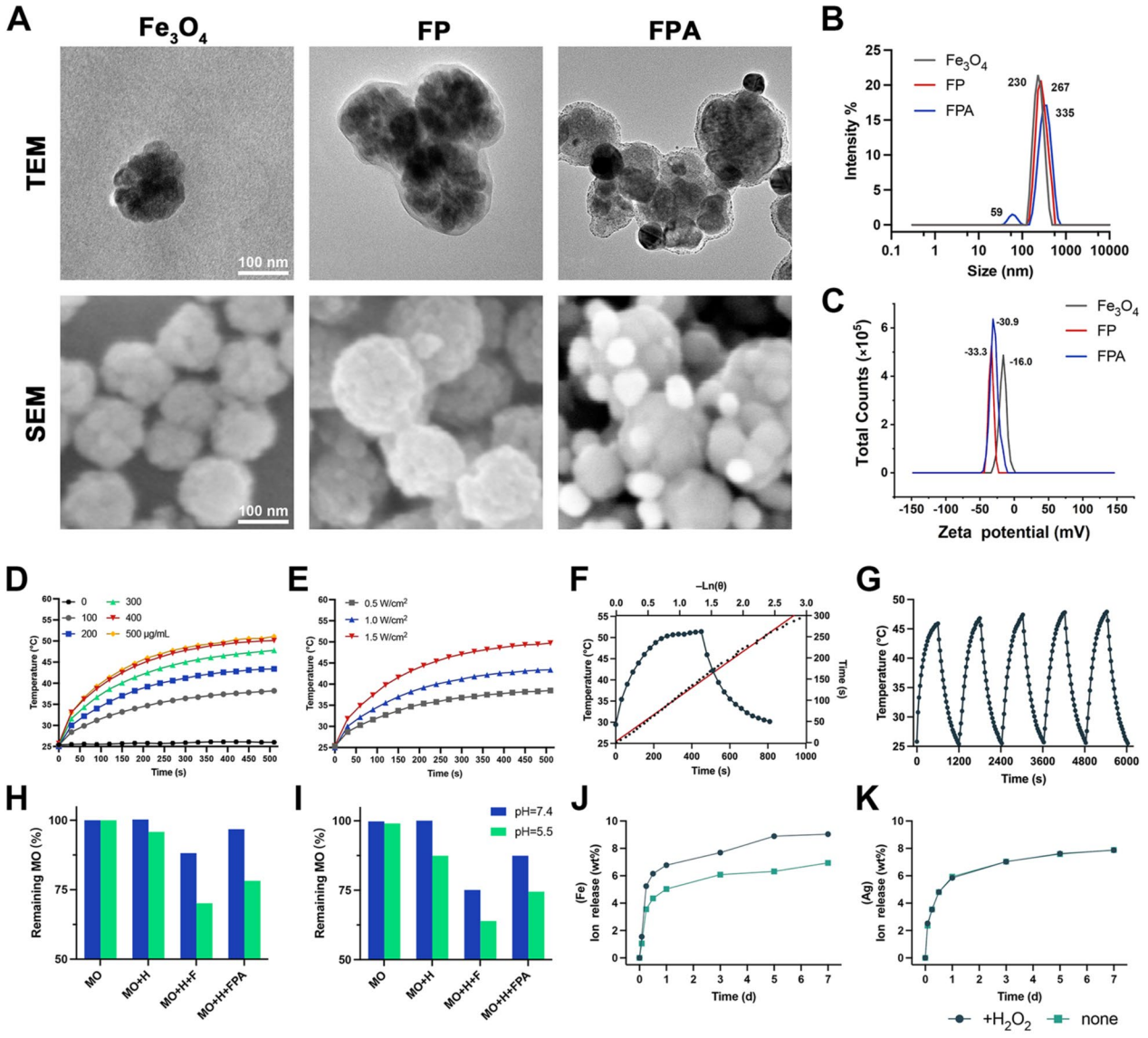

Fig. 1 Characterization of nanoparticles. **A**) TEM and SEM images. **B**) Particle size analysis. **C**) Zeta potential analysis. **D**) Temperature change of different concentrations Fe_3O_4@PDA-Ag suspensions under NIR of 1.0 W cm^{-2}. **E**) Temperature change of Fe_3O_4@PDA-Ag suspension of 200 μg mL^{-1} under NIR of different intensities. **F**) Single temperature-rise – temperature-fall curve and t-Ln (θ) relationship function of Fe_3O_4@PDA-Ag. **G**) Photothermal cycle test of Fe_3O_4@PDA-Ag. **H**, **I**) ROS-promoting effect of the nanoparticles at **H**) 37 °C and **I**) 50 °C under neutral and acidic conditions. **J**, **K**) At pH = 5.5 with or without 0.2 wt % H_2O_2, amount of Fe ions **J**) and Ag ions **K**) released by the Fe_3O_4@PDA-Ag in 7 days

spectrum (Figure S2B), the Fe 2p peak of Fe_3O_4 appeared at a binding energy of 720 eV, whose peak intensity in both Fe_3O_4@PDA and Fe_3O_4@PDA-Ag was reduced by the PDA layer, with an absorption peak of N 1s appearing at 400 eV simultaneously. In addition, an Ag 3d peak appeared at 370 eV in the Fe_3O_4@PDA-Ag spectrum, confirming the presence of Ag NPs.

In the Fourier-transform infrared (FTIR) spectrum (Figure S2C), the characteristic absorption peak of Fe_3O_4 at 536 cm^{-1} corresponds to the stretching vibration of the Fe-O bond. In the Fe_3O_4@PDA spectrum, the characteristic peaks of PDA appeared at 3233 cm^{-1} (O-H and N-H), 1580 cm^{-1} (C=C), 1409 cm^{-1} (N-H), and 1282 cm^{-1} (C-OH). After loading Ag NPs, no new characteristic peaks were observed. As shown in Figure S2D of Raman spectroscopy, for bare Fe_3O_4, the Raman peak at 705 cm^{-1} is attributed to the vibration mode of (Fe-O). For Fe_3O_4@PDA, two peaks were observed at 1347 cm^{-1} and 1570 cm^{-1} owing to the stretching and deformation of the benzene ring in PDA, which Ag further enhanced in Fe_3O_4@PDA-Ag.

Photothermal property assay

We tested the photothermal conversion ability of the nanoparticles using 808 nm near infrared radiation (NIR). The temperatures of each nanoparticles rose continuously for the first 200 s, and finally stabilized at 41℃ (Fe_3O_4), 58℃ (Fe_3O_4@PDA), and 52℃ (Fe_3O_4@PDA-Ag), respectively, whereas the temperatures of H_2O only increased by 1.5℃ (Figure S3). Owing to the excellent photothermal properties of PDA, the final temperature of Fe_3O_4@PDA was significantly higher than that of Fe_3O_4. However, as the shielding effect of the Ag NPs, the temperature of Fe_3O_4@PDA-Ag decreased slightly. Meanwhile, Fe_3O_4@PDA-Ag not only exhibited concentration-dependent (Fig. 1D) and laser density-dependent photothermal (Fig. 1E) conversion characteristics but also had high photostability, which was reflected in the consistent increase in temperature after five cycles of irradiation (Fig. 1G). In addition, the time heat transfer constant τ_s was obtained, 105.27s, and the photothermal conversion efficiency was approximately 30.15% (Fig. 1F and Table S1). In summary, Fe_3O_4@PDA-Ag exhibited a good photothermal conversion effect.

ROS production assay

Under acidic conditions, Fe^{2+} and H_2O_2 undergo the Fenton reaction and eventually produce ·OH. [26] Herein we used the degradation of methyl orange (MO) to detect the generation of ROS (·OH) in simulated bacterial infected tissues that are weakly acidic and presence of H_2O_2in vitro. [43] As shown in Fig. 1H, a few MO were degraded in the presence of only 0.2 wt% H_2O_2 under acidic conditions (pH=5.5). In contrast, after the addition of Fe_3O_4 or Fe_3O_4@PDA-Ag, a significant degradation of MO occurred, apparently due to the generation of ·OH by the reaction between H_2O_2 and the nanoparticles. It was also found that the contact between the inner-core Fe_3O_4 and H_2O_2 may be hindered by the encapsulation of the PDA layer and Ag NPs, resulting in Fe_3O_4@PDA-Ag being less able to promote ROS generation than Fe_3O_4. In addition, we found that at pH=7.4, 0.2 wt% concentration of H_2O_2 barely degraded MO, whereas the same significant degradation of MO occurred after the addition of nanoparticles, but to a lesser extent than under acidic conditions, mainly because H^+ can promote the Fenton reaction and generate more ROS.

However, lower pH conditions cannot be achieved in the bacterial infection microenvironment, thus limiting the rate of ROS production, which can only be mediated by external factors. [44] Given the excellent photothermal conversion of our nanoparticles, this is coincidentally an external factor that can be best controlled. Therefore, we again tested the effects of these nanoparticles on ROS production at 37 °C (physiological temperature) and 50 °C (photothermal temperature). As expected, increasing temperature promoted the Fenton reaction, producing more ROS (Fig. 1I).

Ion release assay

The concentration of Fe ions can affect the Fenton reaction, [45] therefore we continuously measured the amount of Fe ions in the Fe_3O_4@PDA-Ag reaction system. Figure 1J shows that Fe_3O_4 released up to 9 wt% Fe ions throughout 7 d under acidic conditions (pH=5.5) and in the presence of 0.2 wt% H_2O_2, demonstrating that the reaction was ongoing. The release of Ag^+ from Ag NPs during this process is now accepted as an antibacterial mechanism. Therefore, at pH=5.5 and 0.2 wt% H_2O_2, the Ag^+ content of the reaction system was measured. As shown in Fig. 1K, the release of Ag^+ progressed from fast to slow, eventually releasing approximately 8 wt% of the total amount of Ag^+ within 7 days. This indicates that our nanoparticles can continuously release Ag^+ under acidic conditions. In addition, we evaluated the effect of H_2O_2 on ion release and found that the ability of the nanoparticle to release Fe ions was enhanced by H_2O_2, while the ability to release Ag^+ remained almost unchanged. As high H_2O_2 content in IME, this is exactly what we wanted for the infection-microenvironment triggering capability of nanoparticles.

Biocompatibility assay in Vitro

3T3 cells were employed here to evaluate the biocompatibility of nanoparticles. The three groups of nanoparticles (Fe_3O_4, Fe_3O_4@PDA, Fe_3O_4@PDA-Ag) showed the same trend that more than 70% of the cells remained viable when the concentration was kept below 100 μg mL^{-1}, but as the concentration increased, cytotoxicity started to show, especially above 200 μg mL^{-1} (Figure S4). This may be owing to a decreased dispersion in high concentration, and particles accumulating on the cell surface affected the ability of the cells. The increase in Ag^+ concentration in the case of Fe_3O_4@PDA-Ag was also to blame for the decline in cell viability. We assessed the hemolytic activity of the nanoparticles (Figure S5), and the Fe_3O_4 and Fe_3O_4@PDA did not show hemolysis in the concentration range tested. Although we found that Fe_3O_4@PDA-Ag induced hemolysis, it should be noted that this phenomenon only occurred in the high concentration range (>300 μg mL^{-1}). We further performed live/dead and skeletal staining of the cells after 24 h of co-culture with the nanoparticles. No significant cell death was observed in cells co-cultured with the nanoparticles compared to the control group (Figure S6). Similarly, cytoskeletal staining showed the cells in all groups were well expanded and did not undergo any significant morphological changes or shrinkage owing to the addition of the nanoparticles (Figure S7). Overall, these results demonstrate the biosafety of nanoparticles at a range of

concentrations and support their subsequent application in vivo.

Anti-bacterial assay in Vitro

To obtain a preliminary idea of the antimicrobial properties of the nanoparticles, we performed minimal inhibitory concentration (MIC) measurements. Under general conditions (pH = 7.4 without H_2O_2), methicillin-resistant *Staphylococcus aureus* (MRSA) was efficiently suppressed by Fe_3O_4@PDA-Ag at a concentration of approximately 64 μg mL^{-1} (Figure S8A, C). Considering that the nanoparticles were also an excellent Fenton reactant, we tested the MIC values under acidic conditions (pH = 5.5) and in the presence of H_2O_2 (200 μM). Unsurprisingly, the bactericidal ability of Fe_3O_4@PDA-Ag was increased by the dual antibacterial effect, which exhibited bactericidal ability at a concentration of 4 μg mL^{-1} and completely inhibited the growth of MRSA at 8 μg mL^{-1} (Figure S8B, D). In contrast, MRSA was not significantly inhibited only within H_2O_2 or without Ag NPs, which indicates laterally that Fe_3O_4@PDA-Ag has a synergistic effect with the ROS generated by the Fenton reaction in terms of antibacterial activity. Notably, this concentration was well below the cytotoxic concentration (200 μg mL^{-1}).

Anti-bacterial assay with NIR in Vitro

We investigated the enhanced antibacterial activity of nanoparticles under NIR (Fig. 2D). The results demonstrated no difference in bacterial viability in the FP group with or without NIR, it was concluded the photothermal effect of 10 min alone did not effectively inhibit bacterial growth. Contrary, in the presence of Ag NP, the photothermal effect of Fe_3O_4@PDA-Ag enhanced its bactericidal ability, suggesting synergistic in terms of antibacterial activity.

The spread-plate method was employed to assess the antibacterial effectiveness in vitro. (Fig. 2B, E). In both the H_2O_2 and FP groups, the number of colonies was not significantly reduced compared to the control group. However, the quantity of bacteria surviving in the FPA and FPA + H_2O_2 groups was much lower. It is noteworthy that the temperature generated by the photothermal action of the nanoparticles further reduced bacterial survival; however, considering the synergistic effect, this phenomenon was only observed in the FP + H_2O_2, FPA, and FPA + H_2O_2 groups. The live/dead fluorescence staining experiment (Fig. 2C, F) supported the findings that FPA, FPA + H_2O_2, and FP + H_2O_2 treatments, with or without NIR, significantly inhibited bacterial growth or even killed bacteria directly within a short time, as evidenced by the fact that these groups possessed not only fewer green fluorescent particles (live bacteria) but also a larger number and more pronounced red fluorescent particles (dead bacteria).

Figure 2A shows the destructive effect of the nanoparticles on the cell membrane or cell wall of the bacteria. The bacteria exposed to H_2O_2 or Fe_3O_4@PDA, regardless of NIR, retained their normal morphology like the control group (PBS), that is, a smooth and intact spherical surface without the appearance of damage. In contrast, after simultaneous treatment with H_2O_2, Fe_3O_4@PDA, and NIR, the bacteria showed a certain degree of deformation and stretching with irregular contraction and depression of the cell membrane (wall). In both the FPA and FPA + H_2O_2 groups, damage to bacterial cells was more obvious (this phenomenon was more obvious after NIR treatment).

Influence on differentially expressed genes in MRSA

We performed bacterial transcriptome sequencing to explore the possible antimicrobial mechanisms. Sequencing identified 732 differentially expressed genes (DEGs), of which 331 had their expression levels increased, while 401 had it decreased (Fig. 3A). GO functional enrichment analysis revealed that genes associated with MRSA resistance to heat shock, oxidative stress, and energy metabolism functions were all upregulated (Fig. 3C, D), whereas GO functional annotation analysis revealed that the treated bacteria had a significant impact on biological processes, cell components, and molecular functions associated with DEG (Fig. 3E, F).

Previous studies have shown that Ag^+ primarily targets glycolysis and ATP synthesis in *Staphylococcus aureus*. [46] Notably, among the numerous downregulated genes identified, the DEGs focused mainly on energy metabolism-related aspects (Fig. 3C), further confirming the antibacterial role of Fe_3O_4@PDA-Ag via the Ag^+ pathway. Heat shock proteins (HSPs) are an important class of defense proteins that maintain cellular activity when bacteria are exposed to high environmental temperatures. The sequencing results showed that MRSA produced a heat-resistant response after nanoparticle treatment, with significant upregulation of HSP-related genes, confirming that Fe_3O_4@PDA-Ag can be bactericidal via PTT (Fig. 3B). We also observed an upregulation in the expression of dps, rclA, and other related genes encoding antioxidative stress-related proteins that scavenge free radicals and counteract oxidative stress products (Fig. 3B), further indicating that Fe_3O_4@PDA-Ag exerts antimicrobial effects through ROS production. In addition, we observed the downregulation of the expression of genes associated with MRSA virulence factors (crt), cell membrane integrity (cmt), and quorum sensing (Fig. 3B), which have rarely been reported in the mechanism of action of other conventional antimicrobials.

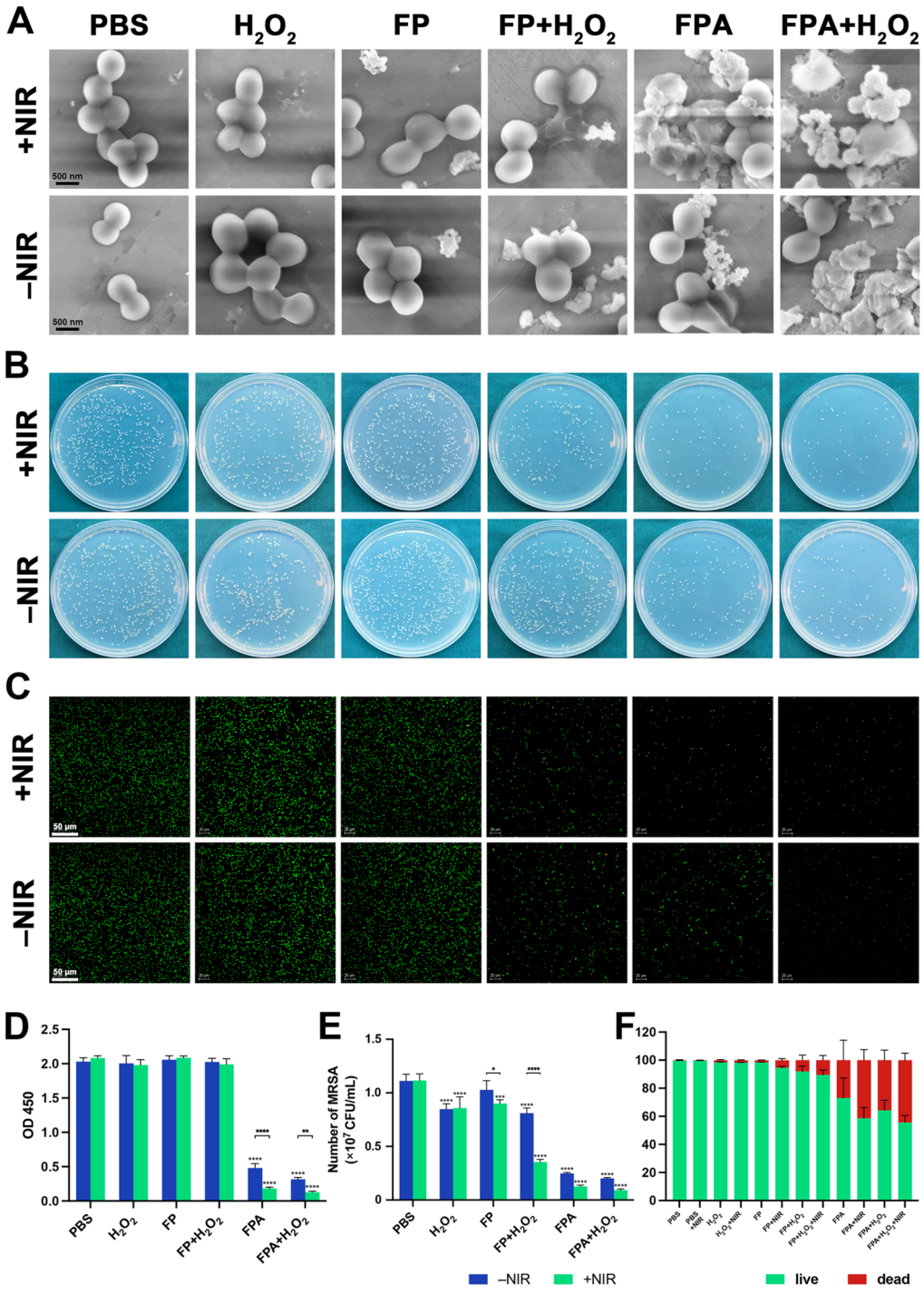

Fig. 2 Evaluation of in vitro antibacterial effect of nanoparticles under NIR. MRSA was mixed with nanoparticles or H_2O_2, irradiated with NIR for 10 min, and continued to co-culture for 2 h. **A**) SEM analysis of the antimicrobial effect of the nanoparticles. **B**, **E**) The plate results after different treatments (means ± SD, $n = 3$, analyzed by two-way ANOVA with Sidak multiple comparisons test). **C**, **F**) The bacterial live/dead staining results after different treatments. **D**) The activity of MRSA mixed with nanoparticles (200 μg mL^{-1}) or/and H_2O_2 at pH = 5.5, irradiated with NIR for 10 min and continued to co-culture for 24 h. (means ± SD, $n = 3$, analyzed by two-way ANOVA with Sidak multiple comparisons test). *$P < 0.05$, **$P < 0.01$, ***$P < 0.001$, ****$P < 0.0001$

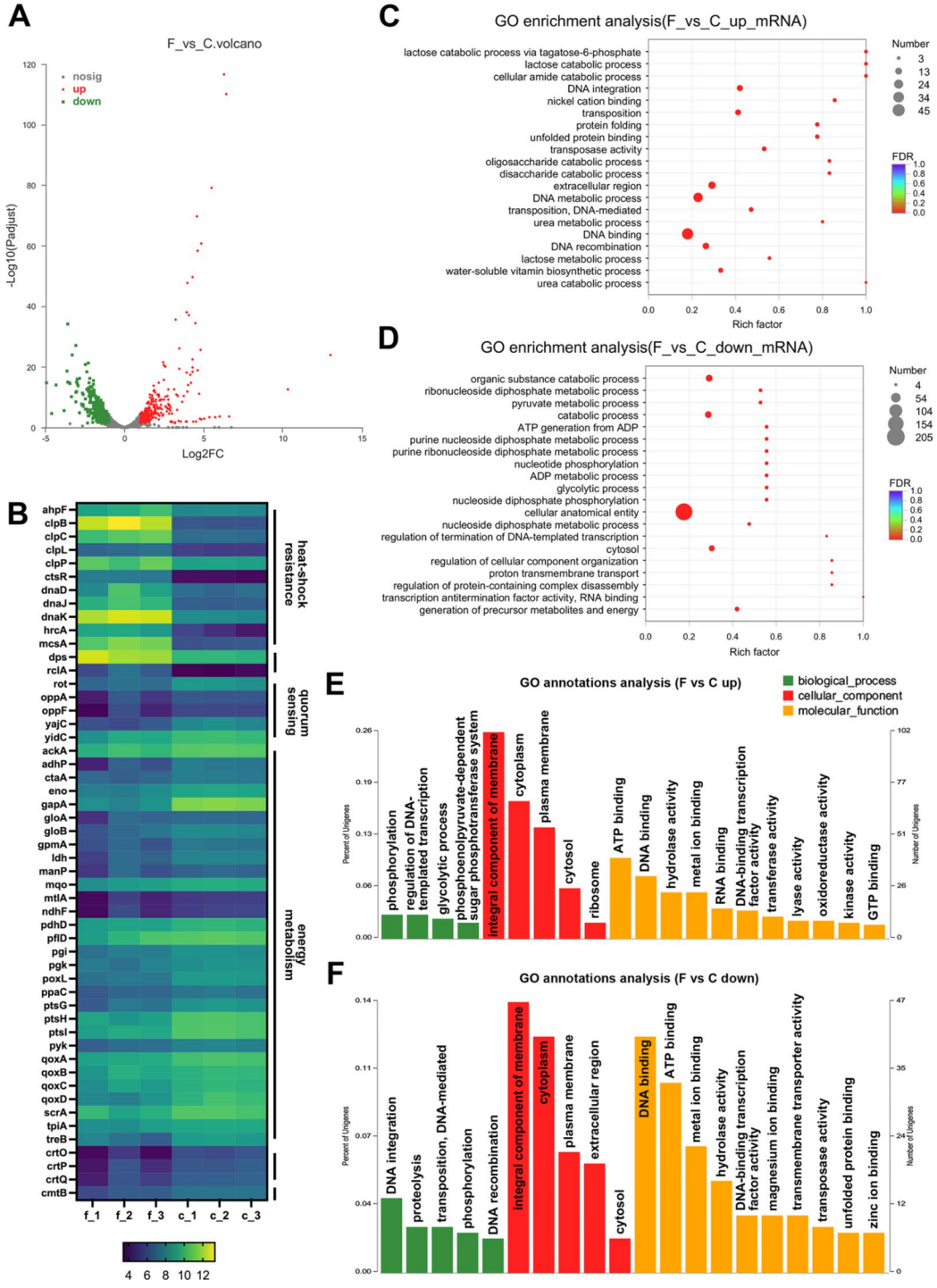

Fig. 3 Changes in the transcriptome of MRSA after treatment with nanoparticles. **A**) Volcano map for the distribution of DEGs. **B**) The DEGs involved in heat-shock resistance, oxidoreductase activity, and quorum sensing of MRSA. **C**, **D**) Upregulated and downregulated DEGs in GO functional enrichment analysis. **E**, **F**) GO annotations analysis of the gene functions of upregulated and downregulated DEGs

Anti-biofilm assay in Vitro

Biofilms are important barriers for bacteria against adverse external environments, and extracellular DNA (eDNA) is an important component for stabilizing the biofilm structure. [47] To our knowledge, ROS has a strong ability to damage DNA. [48, 49] As shown in Fig. 4A, live/dead bacterial fluorescence staining suggested that nanoparticle treatment alone was not effective in disrupting biofilms; however, this effect was slightly enhanced by the addition of H_2O_2. Considering

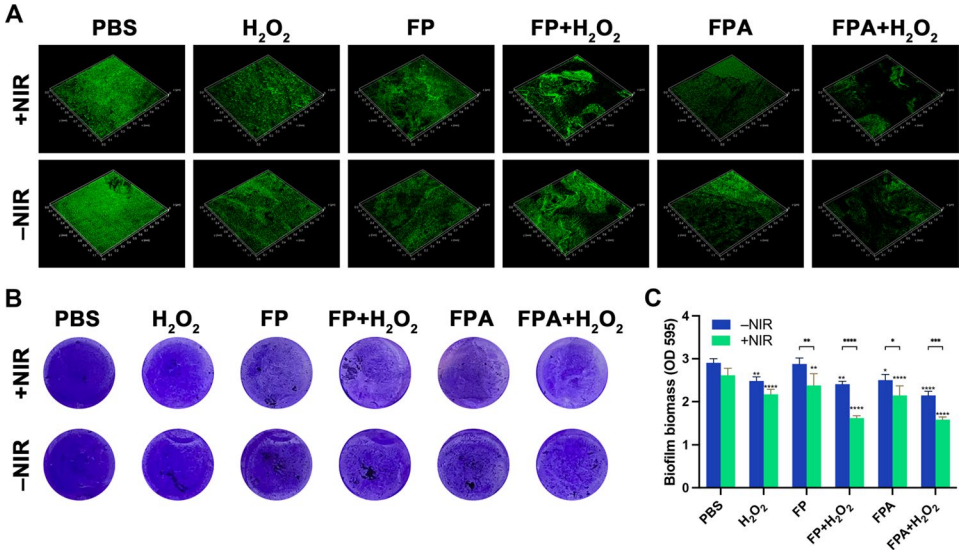

Fig. 4 Evaluation of the effectiveness of different nanoparticles against biofilms. **A**) Live/dead fluorescent staining of bacteria in biofilms after different treatments. Results of **B**) crystal violet staining of biofilms after different treatments and **C**) semi-quantitative statistics (means ± SD, $n = 3$, analyzed by two-way ANOVA with Sidak multiple comparisons test). $^{*}P < 0.05$, $^{**}P < 0.01$, $^{***}P < 0.001$, $^{****}P < 0.0001$

that the green fluorescence signal of the H_2O_2-only group was almost identical to that of the control group, it was confirmed that the ROS was the main factor in the disruption of the bacterial biofilms. It was found that the nanoparticles were more destructive to the biofilm after treatment with NIR than without irradiation. We observed a similar phenomenon in the crystal violet staining results (Fig. 4B, C), where only biofilms treated with both nanoparticles and H_2O_2 were significantly disrupted. NIR further enhanced this effect, may suggesting the synergistic role of photothermal effect in anti-biofilm activity.

Immunomodulatory effects to macrophages

Macrophages are critical in the clearance of infections. In particular, M1 phenotype macrophages exhibit enhanced phagocytic and bactericidal capacities under infectious conditions. [50] Therefore, directing more macrophages toward the M1 phenotype during pathogen invasion is an important means of preventing the development of bacterial infections. It has been reported that nano-silver can initiate M1-like polarization of macrophages for anti-tumor effects via the toll-like receptor 4 signaling pathway. [25] We investigated whether Fe_3O_4@PDA-Ag and Fe_3O_4@PDA could drive macrophage polarization to the M1 phenotype.

We first performed Immunofluorescence (IF) experiments to analyze the expression of inducible nitric oxide synthase (iNOS, highly expressed by M1-type macrophages) and the mannose receptor (CD 206, highly expressed by M2-type macrophages). As shown (Fig. 5A), cells in the FPA and FPA + H_2O_2 groups expressed more iNOS than those in the control and H_2O_2 groups, as evidenced by the fact that they possessed denser and brighter green fluorescence, indicating that macrophages in these two groups were more susceptible to polarization towards M1. In contrast, there was little difference in red fluorescence among the six groups of cells.

In addition, we performed cell flow experiments and obtained similar results (Fig. 5B and Figure S9A). Specifically, cells in the FPA + H_2O_2 and PFA groups possessed the top two ranked CD86 expressions, 11.7%, and 9.15%, respectively, followed by groups of FP + H_2O_2 and FP with 7.41% and 6.16% expression respectively, all higher than those in the H_2O_2, and control groups (4.33% and 3.27%, respectively). In contrast, the percentage of cells expressing CD 206 in these six groups was significantly lower than that of cells expressing CD 86. Our results suggest that Fe_3O_4@PDA-Ag can induce macrophages to polarize towards the M1 pro-inflammatory phenotype, and this effect becomes more pronounced after the addition of H_2O_2.

Finally, we determined the pro-inflammatory cytokines and cellular phenotypic proteins expression level using RT-PCR (Fig. 5C). The expression of intracellular pro-inflammatory-related genes (TNF-α) and genes that mark M1 polarization (CD 86) was upregulated, but there was little difference in the expression of genes related to anti-inflammatory and M2 markers (TGF-β and Arg). Combining these multiple findings, Fe_3O_4@PDA-Ag can indeed influence the differentiation of macrophages towards the M1 phenotype to fight against bacteria.

Macrophage-mediated bactericidal assay

We evaluated the phagocytic activity of macrophages treated with nanoparticles. Although macrophages in all

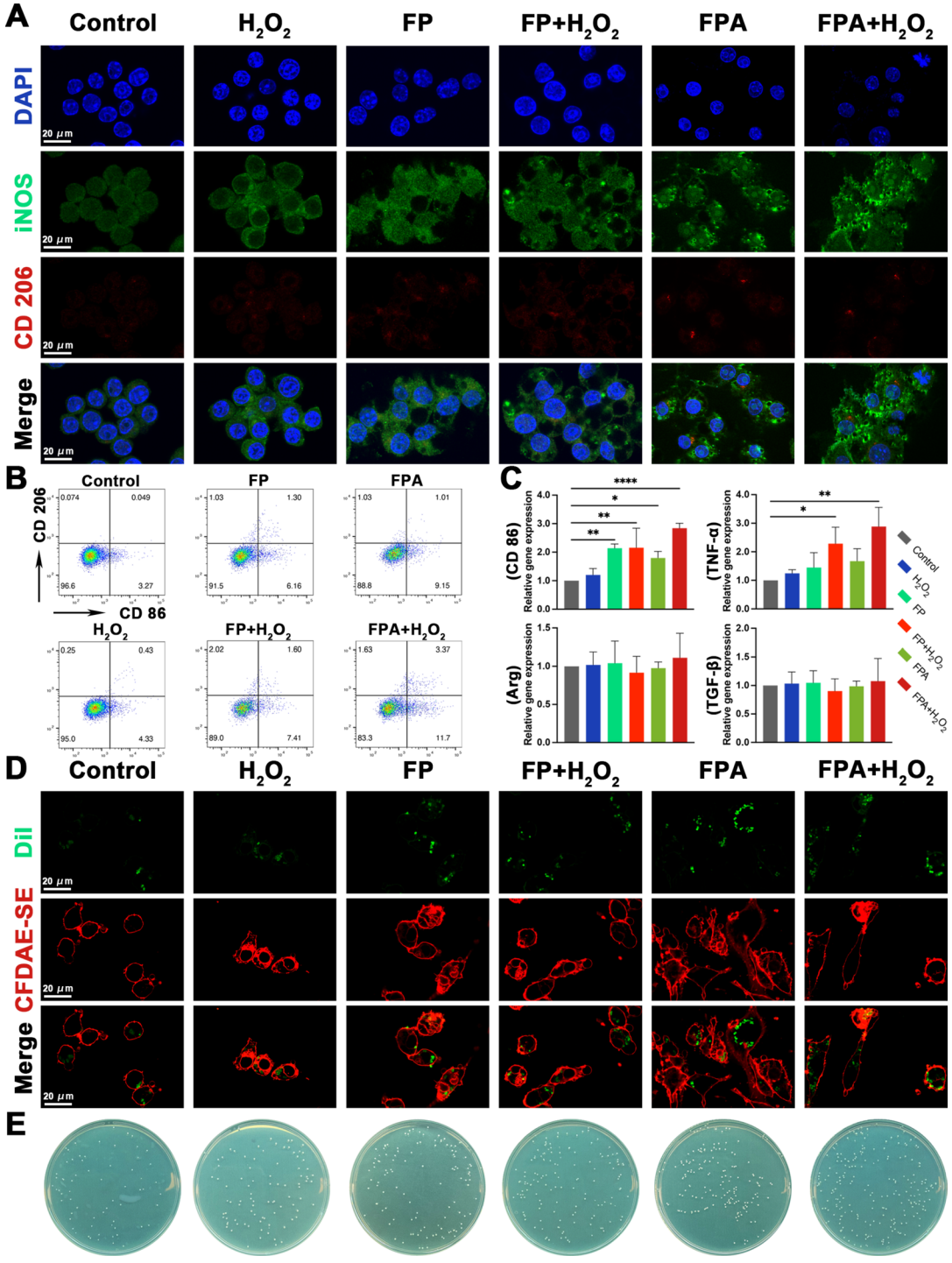

Fig. 5 Evaluation of Fe_3O_4@PDA-Ag and Fe_3O_4@PDA affecting macrophage (RAW 264.7) in vitro. **A**) CLSM assay for M1-tagged proteins (iNOS) and M2-tagged proteins (CD 206). **B**) Representative images of RAW 264.7 surface marker proteins CD 86 and CD 206 by flow cytometry analysis. **C**) Real-time PCR assay of polarization and inflammation-related gene expression in RAW 264.7 (mean ± SD, $n = 3$, analyzed by one-way ANOVA with Dunnett's multiple comparison test). **D**) CLSM observation of nanoparticles treated RAW 264.7 that were co-cultured with CFDA-SE-stained MRSA, and stained with DiI. **E**) Nanoparticles treated RAW 264.7 were co-cultured with MRSA, and the plate result of cell lysate. *$p < 0.05$, **$p < 0.01$, ***$p < 0.001$, ****$p < 0.0001$

groups exhibited some phagocytic activity, macrophages stimulated with FP+H_2O_2 showed greater phagocytosis of MRSA compared to those stimulated with H_2O_2 or FP alone, owing to the enhanced pro-inflammatory effect of ·OH, as evidenced by the fluorescence results (Fig. 5D), where the red circle (macrophage cell membrane) was wrapped around more green fluorescent dots (bacteria). Indeed, we found that macrophages in groups of FPA and PFA+H_2O_2 showed a greater ability to phagocytose bacteria due to the introduction of Ag^+ or/and ·OH. In addition, we performed bacterial colony-forming units (CFU) of macrophage lysates and obtained the same results (Fig. 5E and Figure S9B), that is, more bacteria were phagocytosed by macrophages in the FPA+H_2O_2 or FPA treated group. In summary, we verified that Fe_3O_4@PDA-Ag has a direct antibacterial effect as well as an indirect bactericidal effect by modulating the activity of immune cells.

Antibacterial properties assay in MRSA-infected mouse model

We constructed a mouse skin bacterial infection model to evaluate the antibacterial efficacy of the nanoparticles in vivo and evaluated the temperature at which the skin could rise after NIR (Fig. 6A and Figure S10). Figure 6B shows the changes in the infected tissue from 1 to 7 days after treatment, and the comparison of the abscessed tissue volume in the isolated skin on day 7 (Fig. 6C, E). The mice in both control and FP groups had obvious skin inflammatory edema and the abscess kept getting larger during the 7 days. In contrast, mice injected with Fe_3O_4@PDA-Ag significantly inhibited bacterial growth (little change in abscess within 7 days) and possessed a smaller abscess at 7 days post-treatment. It was noted that the antimicrobial performance of the nanoparticles in vivo was greatly enhanced when it exerted both Fenton and photothermal effects, as the infected tissue in the FPA+NIR group not only possessed minimal volume but even showed signs of healing with surface crusting off at the endpoint of the experimental observation. Then we assessed the number of bacteria remaining in infected skin tissues. The results (Fig. 6D, F) again validate the inhibition of bacteria by Fe_3O_4@PDA-Ag. The antibacterial effect of the FPA was significant, as compared to the control group, but still inferior to the FPA+NIR group. Figure 6G shows the flow chart of our animal experiments.

Subsequently, pathological staining was performed to analyze the infected tissue and the severity of inflammation. The H&E-staining (Fig. 7A) showed that both the PBS and FP groups exhibited a marked inflammatory response, as evidenced by the prominent edematous zone around the abscess, heavily infiltrated with inflammatory cells. In both the FP+NIR and FPA groups, the abscess area was relatively small; therefore, the inflammatory response was relatively mild. In the FPA+NIR group, a synergistic bactericidal effect was exerted, such that almost no abscess tissue was visible, while infection-related inflammation was significantly reduced, and even epidermal tissue undergoing repair could be seen. Giemsa staining (Fig. 7B) revealed significant bacterial residues within the subcutaneous tissue of the control group; however, few bacteria were sporadically visible in the FPA+NIR group.

In addition, we assessed IL-6 expression in infected tissues. In the subcutaneous tissues, IL-6 is an important marker of inflammation, and its higher expression indicates a more severe infection. The staining results (Fig. 7C) further supported these previous findings. The control group, in which infection was not controlled, showed more inflammatory IL-6 positive regions. The next most numerous were in the FP, FP+NIR, and FPA groups, indicating that the infection was somewhat controlled. However, it was not as large as that in the FPA+NIR group, as it possessed the smallest positive area for IL-6. We also assessed the biosafety of the nanoparticles in vivo and did not observe significant pathological changes in the major organs of these mice (Figure S11), as well as significant hepatic or renal impairment (Figure S12).

Polarization and modulation of macrophages in MRSA-infected mouse model

Macrophages play a key role in innate immunity as a defense mechanism against pathogens. Among these, M1 phenotype macrophages are important proinflammatory cells during the early phase of infection that secrete inflammatory factors to kill microorganisms, whereas M2 phenotype macrophages are involved in the anti-inflammatory response and promotion of wound healing during the late phase of infection. [51] In particular, the relatively high temperature can increase the activity of immune cells to enhance the host's immune defense against bacteria. [52, 53] We label different macrophage subtypes at the site of infection in mice to assess the inflammatory response on days 3 and 7 after treatment. According to the results (Fig. 7D), more M1 phenotype cells were present near the infected area in the FPA+NIR group during the progression of infection (day 3), indicating the organism was able to provoke stronger innate immunity to exert an antibacterial effect. In contrast, there were fewer M1 and more M2 macrophages in this group on day 7, suggesting the local inflammatory response was almost controlled, and the organism entered the process of tissue repair. However, the control group did not have sufficient numbers of M1 phenotype cells infiltrating the infected area by day 3, but instead showed more M1 phenotype cells after day 7. The response in the FPA group

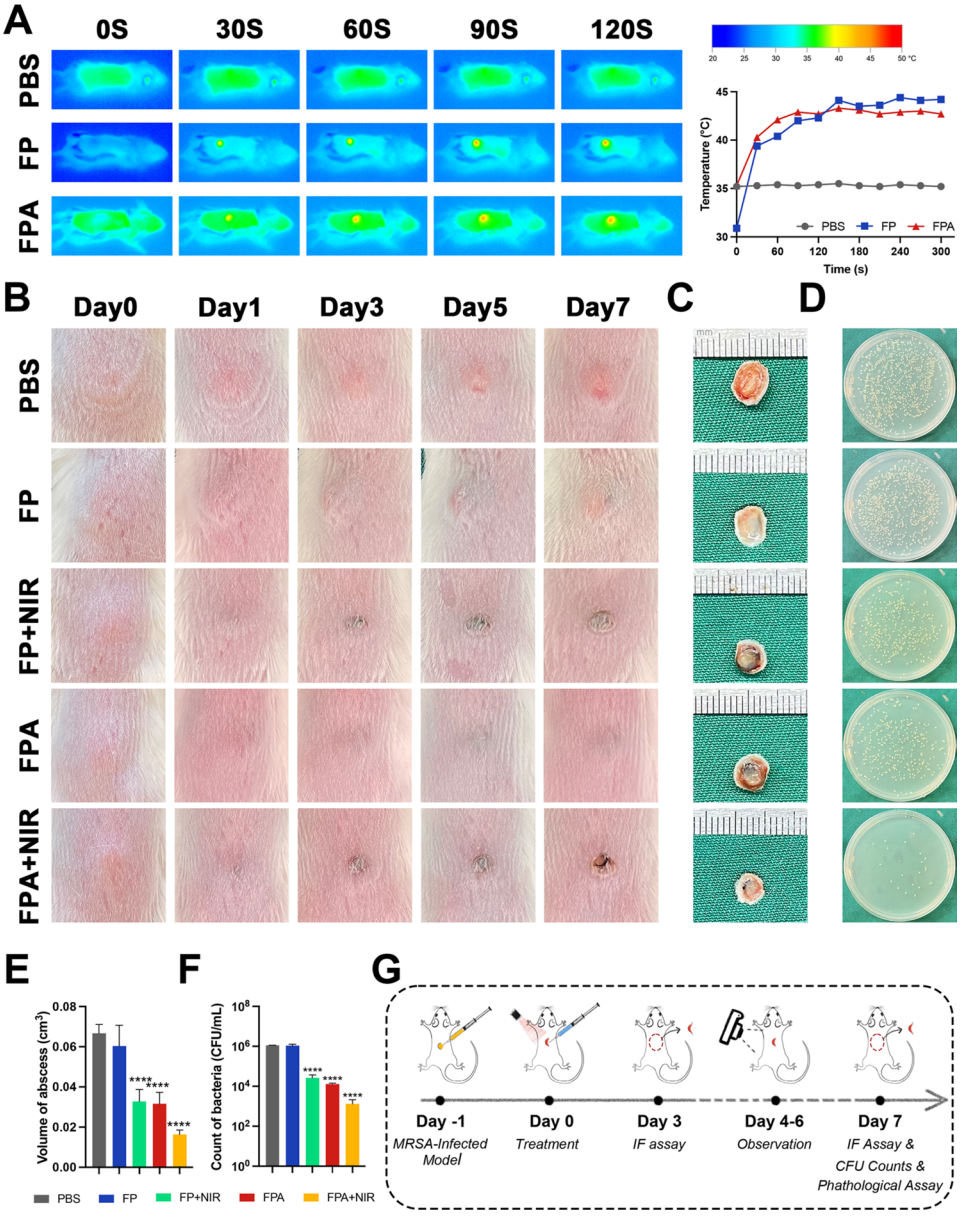

Fig. 6 Treatment results of skin infections in mice. **A**) Skin temperature changes in mice over 300 s. **B**) Representative photographs of skin infection during days 1–7. **C**, **E**) Volumes of skin abscesses on day 7 after treatment (mean ± SD, $n = 3$, analyzed by one-way ANOVA with Dunnett multiple comparisons test). **D**, **F**) Bacterial load assessment of abscess tissue (mean ± SD, $n = 3$, analyzed by one-way ANOVA with Dunnett multiple comparisons test). **G**) Flow chart of animal experiments. $^{*}P < 0.05$, $^{**}P < 0.01$, $^{***}P < 0.001$, $^{****}P < 0.0001$

was intermediate between these two groups. We speculate that in addition to the ability of ROS to regulate cell polarization towards the M1 phenotype, there may be the fact that ROS and NIR together provoke stronger immunogenicity of the pathogen.

Influence on DEGs of cells around infection site

We further performed DEGs analysis of infected tissues at the transcriptome level to search for other possible roles of Fe_3O_4@PDA-Ag in resistance to bacterial infection in vivo. In these two groups, we identified 1375 DEGs (Fig. 8A, B), of which 671 were upregulated and 704 were downregulated. GO enrichment analysis (Fig. 8C, D) revealed the top 20 most enriched functions and pathways. We noted that the DEGs were enriched in phagocytic recognition and engulfment, which supports our previous finding that Fe_3O_4@PDA-Ag promotes macrophage polarization towards the M1 phenotype. In addition, functional enrichment was observed in other immune regulation pathways, including the positive regulation of leukocyte activation, immune response-regulating signaling pathway, B cell receptor signaling

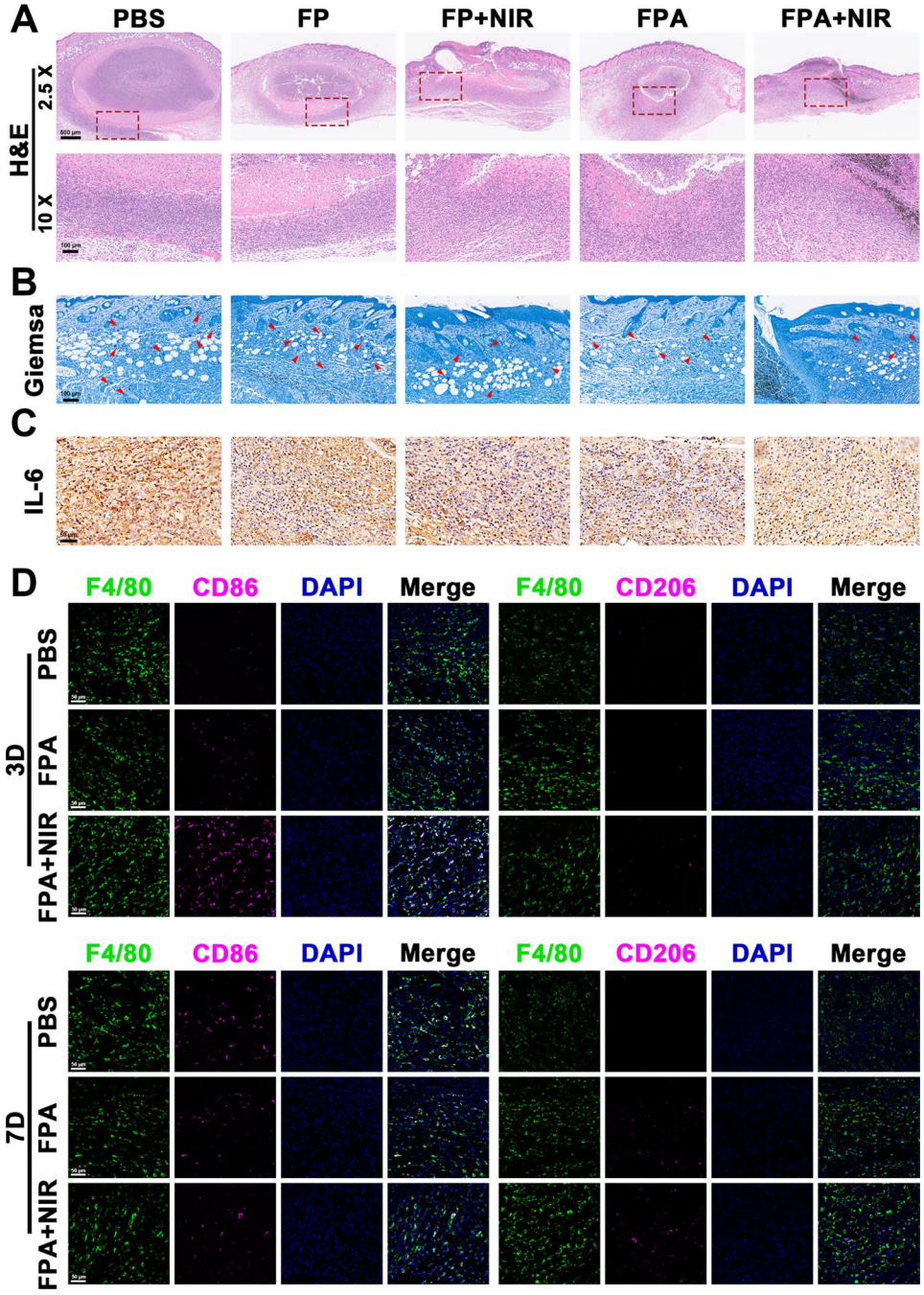

Fig. 7 Histopathological evaluation of the skin. **A**) Representative images of H&E staining. **B**) Representative images of Giemsa staining: circular and darkly stained structures indicate bacteria; red arrows indicate remaining bacteria. **C**) Representative images of IHC staining for IL-6. **D**) Results of labeling different subtypes of cells with IF staining after collecting skin samples on days 3 and 7 after subcutaneous infection of mice treated with nanoparticles. Where co-localization of three signals with F 4/80 (green), CD 86 (red), and DAPI (blue) indicates M1-like cells, and co-localization of three signals with F 4/80, CD 206, and DAPI indicates M2-like cells

pathways, regulation of B cell activation, and antigen receptor-mediated signaling pathways. This indicates that Fe_3O_4@PDA-Ag also positively regulates humoral immunity against bacterial infections.

Here, we proposed a combination of multiple non-antibiotic-dependent antimicrobial modalities against MRSA, which excites us with its excellent antimicrobial, anti-biofilm, and immunomodulatory capabilities. However, there remain certain areas that deserve further investigation. For example, sequencing results in vivo suggest that nanoparticles might play some roles in B cell-based antigen-specific immune responses, but we

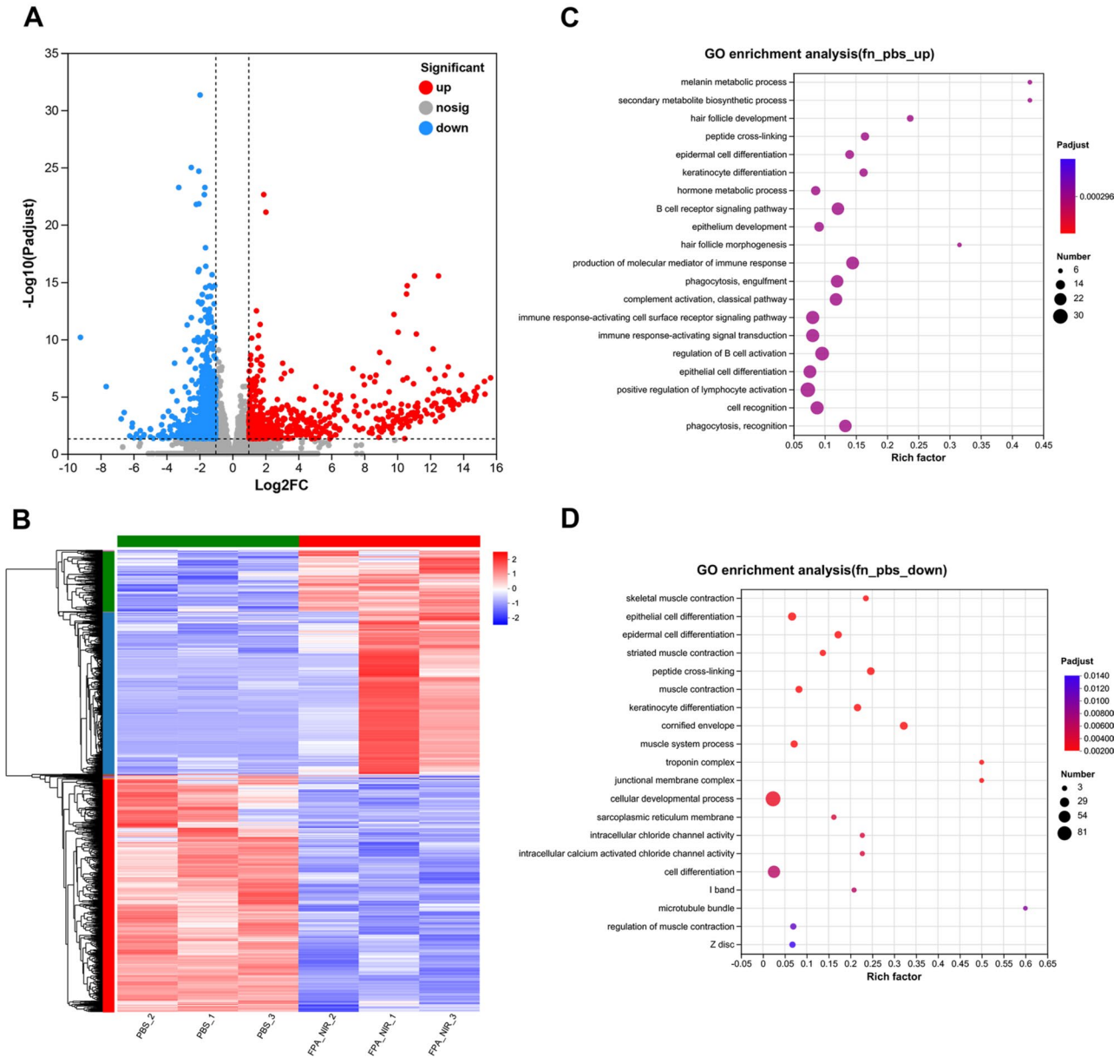

Fig. 8 Transcriptome analysis of the pathway of Fe_3O_4@PDA-Ag against bacterial infection in vivo. **A**) Expression volcano plot of differential genes. **B**) Clustering analysis of differential genes, where red represents genes with up-regulated expression and blue represents genes with down-regulated expression. **C**, **D**) GO functional enrichment analysis of differential genes

did not perform relevant validation to illustrate, so we will focus on this aspect in our future studies. In addition, others have shown that silver nanoparticles affect the phagocytic capacity of neutrophils, thereby reducing the antimicrobial capacity of the innate immune system [54]. Because macrophages, neutrophils, NK cells, and dendritic cells can be involved in the intrinsic immune response, as well as the temporal phasing of the involvement of different cells in the immune response [55], it is necessary to comprehensively consider the effects of nanoparticles on different immune cells in future studies to make a more accurate judgment. Overall, we believe this study provides implications for the management of infections caused by multidrug-resistant bacteria.

Conclusion

In this study, we prepared non-antibiotic-dependent nanoparticles (Fe_3O_4@PDA-Ag) with multimodal synergistic antibacterial ability. The MIC of Fe_3O_4@PDA-Ag against MRSA was only 8 μg mL^{-1} in simulated IME, and NIR-assisted irradiation further enhanced the bactericidal ability. Furthermore, Fe_3O_4@PDA-Ag presents the ability of biofilm disruption along with killing encapsulated bacteria. In addition, Fe_3O_4@PDA-Ag was found

to exert indirect antibacterial effects by promoting macrophages polarizing towards the M1 subtype and secreting cytokines. In animals, Fe_3O_4@PDA-Ag effectively controlled MRSA-induced infections by way of photothermal enhanced CDT, Ag^+ releasing, and innate immunomodulation. Taken together, we successfully prepared Fe_3O_4@PDA-Ag nanoparticles with synergistic antibacterial ability, which is a promising alternative antibacterial agent.

Experimental section

Materials

$FeCl_3{\cdot}6H_2O$, mono-diethylene glycol, ethylene glycol, anhydrous sodium, Tris-HCl buffer, dopamine hydrochloride, polyvinyl pyrrolidone, $AgNO_3$, and methyl orange were obtained from Sigma-Aldrich Trading Co., China. Fetal bovine serum, penicillin-streptomycin, trypsin, PBS, DEME, and α-MEM were obtained from Gibco Life Technologies Co., USA. Cell counting kit-8 (CCK-8), and Microbial Viability Assay Kit were obtained from Dojindo, Japan. Live/Dead Viability/Cytotoxicity Assay Kit was obtained from Thermo Fisher, USA. Actin-Tracker Green-488, DAPI, crystal violet, blocking buffer, CFDA-SE, and cell membrane staining (Dil) were obtained from Beyotime Biotechnology Co., China. Tryptone soya broth (TSB), and mueller-hinton broth (MHB) were obtained from Hope Biotechnology Co., China. RNeasy Mini Kit was obtained from Qiagen, Germany. Primary antibodies (ab210823 and ab64693), and secondary antibodies (ab6785 and ab150080) were obtained from Abcam, GBR. Phycoerythrin (PE)-conjugated anti-F4/80, PE/Cyanine 7-conjugated anti-CD86, and allophycocyanin (APC)-conjugated anti-CD206 were obtained from Biolegeng, USA. PrimeScript RT Master Mix kit and TB Green® Premix Ex Taq™ kit were obtained from Takara, Japan.

Synthesis of Fe_3O_4

Synthesis of Fe_3O_4 nanoparticles using a solvothermal method. Briefly, 0.54 g $FeCl_3{\cdot}6H_2O$ was dissolved in a solution of 15 mL of mono-diethylene glycol and 5 mL of ethylene glycol. Then 1.5 g of anhydrous sodium acetate was added under stirring for 1 h, followed by sonication for 30 min, and transferred to the reactor at 200 °C for 10 h. After cooling, washing, and drying, Fe_3O_4 was obtained.

Synthesis of Fe_3O_4@PDA

100 mg Fe_3O_4 was added to 50 mL Tris-HCl buffer and sonicated for 30 min. Then, 60 mg of dopamine hydrochloride in a 10 wt% aqueous solution was added and stirred for another 12 h. Finally, Fe_3O_4@PDA was obtained after centrifugation and washing, and dispersed in 10 mL of ethanol.

Synthesis of Fe_3O_4@PDA-Ag

Ag NPs were first synthesized by dissolving 500 mg of polyvinyl pyrrolidone and 130 mg of $AgNO_3$ in 37 mL of ethanol with stirring and then transferring to the reactor for 3 h. After cooling, centrifugation, and washing, Ag NP suspension was obtained. The dispersed Fe_3O_4@PDA nanoparticle was added into Ag NPs suspension and stirred for 2 h. When the reaction was over, the Fe_3O_4@PDA-Ag was washed, separated by the magnet, and dried in a vacuum oven at 60 °C.

Characterization of nanoparticles

Morphological characterization of NPs was performed using TEM (HT7700, Hitachi, JPN), SEM (Regulus 8230, Hitachi, JPN), XPS (Escalab 250Xi, Thermo Scientific, USA), XRD (Max-2550, Rigaku, JPN), Raman spectroscopy (inVia-Reflex, Renishaw, GBR), and FTIR spectroscopy (Nicolet iS50, Thermo Scientific, USA). The hydrodynamic diameter and zeta potential of the NPs were measured using a laser particle size analyzer (Zetasizer Pro, Malvern, GBR).

Photothermal Conversion Effect

The photothermal conversion effect of nanoparticles was evaluated in vitro using an NIR laser system, and the temperature change was recorded using an infrared thermographer. Fe_3O_4, Fe_3O_4@PDA, and Fe_3O_4@PDA-Ag were dispersed in pure water at a concentration of 1 mg mL^{-1} and irradiated with a laser at 1 W cm^{-2} for 500 s. The photothermal conversion effect of Fe_3O_4@PDA-Ag was measured at different concentrations (100, 200, 200, 300, 400, and 500 μ mL^{-1}) and power densities (0.5, 1.0, and 1.5 Wcm^{-2}). The Fe_3O_4@PDA-Ag suspension reached a maximum temperature after irradiation, followed by turning off the laser for natural cooling, and the irradiation was repeated under the same condition again, and then repeatedly. Finally, the temperature-rise – temperature-fall curve was plotted, and the following equations were used to calculate photothermal conversion efficiency:

$$\eta = \frac{hS\left(T_{max} - T_{surr}\right) - Q_{dis}}{I\left(1 - 10^{-A_\lambda}\right)} \tag{1}$$

$$\tau_s = \frac{m_d C_d}{hS} \tag{2}$$

$$t = -\tau_s \ln\theta \tag{3}$$

$$\theta = \frac{T_{surr} - T}{T_{surr} - T_{max}} \tag{4}$$

ROS production assay in vitro

MO solutions of 10 mg L^{-1}, 0.6 wt% H_2O_2 solution, 300 μg mL^{-1} Fe_3O_4 solution and 300 μg mL^{-1} Fe_3O_4@PDA-Ag suspension were prepared consecutively. Different reaction systems (group MO, group MO+H_2O_2, group MO+H_2O_2+Fe_3O_4, and group MO+H_2O_2+Fe_3O_4@PDA-Ag were set up, followed by sonication for 5 min, and then placed at 37 °C and 50 °C to react. The absorbance of the filtered solution without nanoparticles was measured at 464 nm using an ultraviolet spectrophotometer (SPECOR210, Analytic Jena, DEU) and the degradation ratio was calculated to indirectly reflect the ROS concentration.

Ion release assay

Fe_3O_4@PDA-Ag nanoparticles were dispersed in 10 mL of acidic PBS buffer (pH=5.5) containing 60 μL of 30% H_2O_2 and stirred at low speed at a constant temperature of 37 °C. At specific time points (2 h, 4 h, 6 h, 12 h, 1d, 2d, 3d and 7d), 5 ml of supernatant was collected, and the contents of ferrous and silver ions were measured by inductive coupled plasma (ICP) emission spectrometer (Prodigy Plus, Leeman, FRA) to calculate the ion release rate, after which 5 ml of PBS buffer (pH=5.5) and 30 μL of 30% H_2O_2 solution were added.

Biocompatibility of nanoparticles

Fresh mouse blood was used to assess hemolysis. [56] Briefly, collected and prepared 4% (v/v) red blood cell suspension in PBS at 4 °C. Then the red blood cell suspensions were added to the same volume of suspensions (20, 40, 100, 200, 400, 600, and 1000 μg mL^{-1}) of Fe_3O_4, Fe_3O_4@PDA, and Fe_3O_4@PDA-Ag, and incubated at 37℃ for 2 h. Finally, the absorbance of the supernatants was measured at 540 nm (Triton-X was used as the positive control and PBS as the negative control group). The hemolysis rate was calculated using the following equation:

$$\text{Hemolysis } (\%) = \frac{A_{\text{sample}} - A_{\text{PBS}}}{A_{\text{Triton}} - A_{\text{PBS}}} \times 100\% \quad (5)$$

The cytotoxicity of the nanoparticles was evaluated using CCK-8 reagent. Briefly, 3T3 cells were seeded in 96-well plates at a density of 5×10^4 cells per well. After 24 h, the cell culture medium was replaced with suspensions of Fe_3O_4, Fe_3O_4@PDA, and Fe_3O_4@PDA-Ag at concentrations of 0, 10, 20, 50, 100, 200, 300, and 500 g mL^{-1}. A culture medium containing 10% CCK-8 reagent was used to culture the cells for 2 h on Day 1. Finally, the supernatant was collected, and the absorbance at 450 nm was measured. After incubation with 200 g mL^{-1} Fe_3O_4, Fe_3O_4@PDA, and Fe_3O_4@PDA-Ag for 24 h, the cells were stained with Live/Dead Viability/Cytotoxicity Assay Kit (Beyotiome, CHN) and then observed under confocal laser scanning microscopy (CLSM, FV3000, Olympus, JPN). For morphological assessment, cells treated under the same conditions were stained with Actin-Tracker Green-488 (Beyotiome, CHN) and DAPI (Beyotiome, CHN) consecutively, and images were obtained by CLSM.

Bacterial culture and MIC assay

MRSA was purchased from ATCC, and individual colonies were picked from LB agar plates and added to fresh tryptone soya broth (TSB) bacterial medium. The bacterial suspension was diluted 1:100 after shaking (200 rpm) overnight at 37 °C, and shaken for another 4 h to allow the bacteria to be in the logarithmic growth phase. Bacteria were diluted to 2×10^6 CFU mL^{-1} with mueller-hinton broth (MHB) and added to 96-well plates at a volume of 100 μL per well. After that, different concentrations (1.95, 3.91, 7.81, 15.6, 31.3, 62.5, 125, 250, 500, and 1000 μg mL^{-1}) of Fe_3O_4, Fe_3O_4@PDA or Fe_3O_4@PDA-Ag were mixed with bacteria in equal volume, respectively. After incubation in a constant temperature incubator at 37 °C for 24 h, the turbidity of the wells was observed to derive the MIC of the nanoparticles. Bacterial viability was tested using a Microbial Viability Assay Kit (Dojindo, JPN). MIC values under acidic and H_2O_2 (200 μM) conditions were measured using the method described above.

Anti-bacterial assay with NIR in vitro

12 groups with or without NIR were set up: PBS, H_2O_2, FP, FP+H_2O_2, FPA, and FPA+H_2O_2 (nanoparticles of 200 μg mL^{-1}, H_2O_2 of 200 μM, NIR intensity of 1.0 W cm^{-2} with 10 min). The treated bacteria of each group were serially diluted 1000-fold, then 10 μL of which was spread onto LB plates. After incubation at 37 °C for 18 h, CFUs were imaged and counted. For live/dead staining, after bacteria were treated in the same way, 100 μL mixed SYTO9 and PI dyes (live/dead BacLight bacterial viability kit, Invitrogen, USA) were added for staining according to the specification. Bacteria were observed by CLSM. Besides, bacteria after the same treatment were collected, and fixed with 2.5% glutaraldehyde at 4 °C overnight. The samples were then serially dehydrated for 10 min in alcohol at different concentration gradients (30%, 40%, 50%, 60%, 70%, 80%, 90%, and absolute ethanol), followed by freeze-drying, sputter coating with gold, and SEM observation.

RNA sequencing of MRSA

The total RNA of MRSA was extracted after treatment with Fe_3O_4@PDA-Ag (200 μg mL^{-1}), H_2O_2 (200 μM), and NIR (1.0 W cm^{-2}, 5 min) using RNeasy Mini Kit (Qiagen, DEU), and sent to Shanghai Meiji Biomedical Technology Co. under drikold protection for sequencing work

by Illumina Hiseq. The expression levels of genes were quantified separately using RSEM expression quantification software. Gene Ontology (GO) enrichment analysis was performed on genes in the gene set using Goatools software to obtain GO functions. A corrected P value (P-adjust) of <0.05 was used as a Fisher's exact test, and the GO function was considered to be significantly enriched when P-adjust was <0.05.

Dispersion of established biofilm

100 μL of bacteria at a concentration of 1×10^7 CFU mL^{-1}, in the logarithmic growth stage, were added to the well plate, cultured overnight at 37℃, then replaced with new medium and cultured for another 24 h, to establish biofilm. [57] Next, the medium containing the unattached bacteria was removed, and the cells were washed gently with PBS three times. Twelve groups with or without NIR were set up: PBS, H_2O_2, FP, FP+H_2O_2, FPA, and FPA+H_2O_2 (nanoparticles 200 μg mL^{-1}, H_2O_2 200μM). After irradiation (1 W cm^{-2}) for 10 min, the biofilms were washed, fixed, and stained with 0.1% crystal violet for 30 min. After the biofilm was dried and imaged, crystal violet was dissolved in ethanol and its absorbance was measured at 595 nm. Additionally, mixed SYTO9 and PI dyes were used to observe the fluorescence-based biofilms using CLSM.

Immunomodulatory effects of nanoparticles

The Polarization of macrophages towards M1 and M2 was detected using IF, flow cytometry, and real-time PCR (RT-PCR). [58] Briefly, RAW 264.7 cells were inoculated on confocal dishes at a density of 2×10^5 cells per well for 24 h, followed by co-culture with nanoparticle, H_2O_2 or nanoparticle+H_2O_2 (100 μg mL^{-1} for both FPA and FP, 200 μM for H_2O_2), and set without any nanoparticles or reagent as the control group. After another 24 h, the cells were gently washed with PBS and subjected to 4% paraformaldehyde fixation, Triton X-100 permeabilization, and treated with a blocking buffer. Subsequently, the specimens in each group were incubated with primary antibodies overnight at 4 °C and stained with secondary antibodies for 1 h, away from light, and then the nuclei were re-stained with DAPI for 10 min before observation under CLSM. For the flow cytometry assay, RAW 264.7 cells after treatment with the same method, were collected, washed with PBS three times, and made into single cell suspensions using PBS containing 2% fetal bovine serum. Next, the cells were labeled with phycoerythrin (PE)-conjugated anti-F4/80, PE/Cyanine 7-conjugated anti-CD86, and allophycocyanin (APC)-conjugated anti-CD206 on ice for 30 min, away from light, and then analyzed using a flow cytometer (DxFLEX, Beckman, USA). For RT-PCR, total RNA from cells treated with the above method was extracted and then reverse transcribed into cDNA for subsequent RT-PCR assays. The forward and reverse primers for the target genes were synthesized by Shanghai Bioengineering Co., Ltd. The base sequences are shown in Table S2, and the housekeeping gene-actin was used as an internal reference for the comparison of target genes using a relative quantitative method.

Macrophage-mediated bactericidal assay

Macrophage-mediated bactericidal activity was assessed with CLSM and tissue plate assay. Briefly, RAW 264.7 cells were inoculated on confocal dishes at a density of 2×10^5 cells per well for 24 h, followed by co-culture with nanoparticle, H_2O_2, or nanoparticle+H_2O_2 (100 μg mL^{-1} for both FPA and FP, 200 μM for H_2O_2), and set without any nanoparticles or reagent as the control group. After 24 h, the particles were washed off and the bacterial (which had been stained with CFDA-SE for 1 h) suspension of 1×10^7 CFU mL^{-1} was added to co-culture with the cells for 8 h. Next, the medium containing vancomycin (2 μg mL^{-1}) was changed, the cells were incubated for another 1 h and then washed three times with PBS to remove non-phagocytosed bacteria. The cells were then fixed with 4% paraformaldehyde, permeabilized with 0.1% Triton X-100 solution, and stained with a cell membrane staining (Dil) working solution in the dark. Finally, the samples were placed under CLSM for observation and photography. In addition, we quantified phagocytosed bacteria. Macrophages with phagocytosed bacteria were lysed using sterile distilled water. This was followed by diluting and coating the lysate on LB plates, which were incubated at 37 °C for 24 h, then photographed, and the number of CFU was calculated.

Animal experiments

All BALB/c mice were purchased from JSJ Lab (Shanghai, China), and the Animal Ethics Committee of Renji Hospital, Shanghai Jiao Tong University School of Medicine approved the use of animals in research. A mouse model of MRSA skin infection was established according to a previous publication. [59] Specifically, the dorsal side of the pentobarbital-anesthetized mice was shaved, followed by skin disinfection with 70% ethanol at the intended inoculation site. The mice were then subcutaneously inoculated with 50 μL of 1×10^7 MRSA during the logarithmic growth phase. After 24 h and formation of abscess, mice were divided randomly into five groups and were given different treatments as follows: (1) PBS (50 μL); (2) Fe_3O_4@PDA; (3) Fe_3O_4@PDA+NIR; (4) Fe_3O_4@PDA-Ag; (5) Fe_3O_4@PDA-Ag+NIR, among which the concentrations of the nanoparticles were all 2 mg mL^{-1} in 50 μL. After the local injection of the nanoparticles, the abscess was irradiated by NIR (1.0 W cm^{-2}, 5 min) immediately. The infected area of each mouse was photographed before all mice were sacrificed on day 7 after

treatment, and skin tissues or organs were collected to evaluate the infection status (hematoxylin and eosin [H&E] staining, Giemsa staining, and immunohistochemistry), immunomodulatory effects (IF), or toxicity (H&E staining). The length and width of the abscess were measured and used to calculate the abscess volume

$$V = \frac{4}{3}\pi \times \left(\frac{L}{2}\right)^2 \times \frac{W}{2} \quad (6)$$

For the immunomodulatory effect assay, skin tissues from group PBS, group Fe_3O_4@PDA-Ag, and group Fe_3O_4@PDA-Ag+NIR were collected on days 3 and 7.

RNA sequencing of tissue

Three biological replicates of skin tissue samples from group PBS and group Fe_3O_4@PDA-Ag+NIR were collected and sent them to Shanghai Meiji Biomedical Technology Co. under Drikold protection for subsequent sequencing. Software DESeq2 was used for the differential expression, and a gene was considered as a differentially expressed gene (DEG) when it met both screening criteria (FDR < 0.05 & |log2FC| > 1). GO enrichment analysis was performed using Fisher's exact test. To control the calculated false positive rate, the P-adjust was corrected using four multiplex tests (Bonferroni, Holm, Sidak, and false discovery rate), and a GO function was considered significantly enriched when the p-adjust was < 0.05.

Statistical analysis

Biological replicas were used in all investigations. The software Prism 9 (GraphPad Software Inc., CA, USA) was used to examine the outcomes. Data are expressed as mean ± standard deviation (SD). The sample size (n) and data preprocessing are given in the corresponding figure legends. One-way analysis of variance (ANOVA) or two-way ANOVA was used to identify samples where there were significant differences. P value < 0.05 to indicate statistical significance ($^{*}p<0.05$, $^{**}p<0.01$, $^{***}p<0.001$, $^{****}p<0.0001$).

Supplementary Information

The online version contains supplementary material available at https://doi.org/10.1186/s12951-024-02706-y.

Supplementary Material 1

Acknowledgements
Not applicable.

Author contributions
Q. H., W. Z. and Z. L. contributed equally to this work. Q. H.: Methodology, Validation, Formal analysis, Investigation, Writing -original draft. W. Z. and Z. L.: Methodology, Validation, Formal analysis, Investigation, Writing - original draft. B. L. and R. W.: Methodology, Validation, Formal analysis, Investigation. X. L. and Z. W.: Validation, Investigation. J.Y., B. N. and B. Y.: Conceptualization, Resources, Formal analysis, Writing - review & editing. All authors reviewed the manuscript.

Funding
This work was supported by the National Natural Science Foundation of China (No. No. 81972086, 82372422, and No. 82172464).

Data availability
No datasets were generated or analysed during the current study.

Declarations

Ethics approval and consent to participate
All animal experiments followed the Guidelines for the Care and Use of Laboratory Animals at Renji Hospital and were approved by the Renji Hospital Animal Ethics Committee (Ethics No.2023 – 465).

Consent for publication
Not applicable.

Competing interests
The authors declare no competing interests.

Author details
[1]Department of Bone and Joint Surgery, Department of Orthopedics, Renji Hospital, School of Medicine, Shanghai Jiaotong University, Shanghai 200127, China
[2]State Key Laboratory for Modification of Chemical Fibers and Polymer Materials, College of Materials Science and Engineering, Donghua University, Shanghai 201620, China
[3]Key Laboratory of Carcinogenesis and Translational Research (Ministry of Education), Department of Radiology, Peking University Cancer Hospital & Institute, Beijing 100142, China

Received: 24 April 2024 / Accepted: 5 July 2024
Published online: 30 July 2024

References

1. Murray CJL, Ikuta KS, Sharara F, Swetschinski L, Aguilar GR, Gray A, et al. Global burden of bacterial antimicrobial resistance in 2019: a systematic analysis. Lancet. 2022;399(10325):629–55.
2. Yin J, Wang Y, Xu X, Liu Y, Yao L, Sun Q. The progress of global antimicrobial resistance governance and its implication to China: a review. Antibiot (Basel). 2021;10(11):1356.
3. Soltani J, Versporten A, Goossens H. Antibiotic resistance: a global concern; current situation and action plans. Erciyes Med J. 2019;41(2):125–7.
4. Liu J, Gefen O, Ronin I, Bar-Meir M, Balaban NQ. Effect of tolerance on the evolution of antibiotic resistance under drug combinations. Science. 2020;367(6474):200–4.
5. Koo H, Allan RN, Howlin RP, Stoodley P, Hall-Stoodley L. Targeting microbial biofilms: current and prospective therapeutic strategies. Nat Rev Microbiol. 2017;15(12):740–55.
6. Goff DA, Kullar R, Goldstein EJC, Gilchrist M, Nathwani D, Cheng AC, et al. A global call from five countries to collaborate in antibiotic stewardship: united we succeed, divided we might fail. Lancet Infect Dis. 2017;17(2):e56–63.
7. Fleming-Dutra KE, Hersh AL, Shapiro DJ, Bartoces M, Enns EA, File TM Jr., et al. Prevalence of inappropriate antibiotic prescriptions among US ambulatory care visits, 2010–2011. JAMA. 2016;315(17):1864–73.
8. Costerton JW, Stewart PS, Greenberg EP. Bacterial biofilms: a common cause of persistent infections. Science. 1999;284(5418):1318–22.
9. Davies D. Understanding biofilm resistance to antibacterial agents. Nat Rev Drug Discov. 2003;2(2):114–22.
10. Su Z, Kong LT, Mei JW, Li QM, Qian ZZ, Ma YY, et al. Enzymatic bionanocatalysts for combating peri-implant biofilm infections by specific heat-amplified chemodynamic therapy and innate immunomodulation. Drug Resist Updates. 2023;67:1189.
11. Qi Y, Ren SS, Ye JW, Tian YM, Wang GY, Zhang SQ, et al. Infection microenvironment-activated core-shell nanoassemblies for photothermal/chemodynamic

synergistic wound therapy and multimodal imaging. Acta Biomater. 2022;143:445–58.
12. Xu MM, Tan FR, Luo WR, Jia YF, Deng Y, Topham PD, et al. In situ fabrication of silver peroxide hybrid ultrathin co-based metal-organic frameworks for enhanced chemodynamic antibacterial therapy. ACS Appl Mater Inter. 2023;15(19):22985–98.
13. Zheng W, Sun W, Simeonov A. Drug repurposing screens and synergistic drug-combinations for infectious diseases. Br J Pharmacol. 2018;175(2):181–91.
14. Sun W, Sanderson PE, Zheng W. Drug combination therapy increases successful drug repositioning. Drug Discov Today. 2016;21(7):1189–95.
15. Mi GJ, Shi D, Wang M, Webster TJ. Reducing bacterial infections and biofilm formation using nanoparticles and nanostructured antibacterial surfaces. Adv Healthc Mater. 2018;7(13):e1800103.
16. Linklater DP, Baulin VA, Juodkazis S, Crawford RJ, Stoodley P, Ivanova EP. Mechano-bactericidal actions of nanostructured surfaces. Nat Rev Microbiol. 2021;19(1):8–22.
17. Wang Y, Yang YN, Shi YR, Song H, Yu CZ. Antibiotic-free antibacterial strategies enabled by nanomaterials: progress and perspectives. Adv Mater. 2020;32(18):e1904106.
18. Pelgrift RY, Friedman AJ. Nanotechnology as a therapeutic tool to combat microbial resistance. Adv Drug Deliv Rev. 2013;65(13–14):1803–15.
19. Tang HZ, Qu XH, Zhang WK, Chen X, Zhang ST, Xu Y, et al. Photosensitizer nanodot eliciting immunogenicity for photo-immunologic therapy of postoperative methicillin-resistant *Staphylococcus aureus* infection and secondary recurrence. Adv Mater. 2022;34(12):e2107300.
20. Qu XH, Wang MQ, Wang MC, Tang HZ, Zhang ST, Yang HT, et al. Multi-mode antibacterial strategies enabled by gene-transfection and immunomodulatory nanoparticles in 3D-printed scaffolds for synergistic exogenous and endogenous treatment of infections. Adv Mater. 2022;34(18):e2200096.
21. Sun CX, Wang XB, Dai JJ, Ju YM. Metal and metal oxide nanomaterials for fighting planktonic bacteria and biofilms: a review emphasizing on mechanistic aspects. Int J Mol Sci. 2022;23(19):11348.
22. Zhao XH, Tang H, Jiang XY. Deploying gold nanomaterials in combating multi-drug-resistant bacteria. ACS Nano. 2022;16(7):10066–87.
23. Li D, Kumari B, Makabenta JM, Tao BL, Qian K, Mei XF, et al. Development of coinage metal nanoclusters as antimicrobials to combat bacterial infections. J Mater Chem B. 2020;8(41):9466–80.
24. Buszewski B, Railean-Plugaru V, Pomastowski P, Rafinska K, Szultka-Mlynska M, Golinska P, et al. Antimicrobial activity of biosilver nanoparticles produced by a novel *Streptacidiphilus durhamensis* strain. J Microbiol Immunol. 2018;51(1):45–54.
25. Yan X, Qi Y, Ren LT, Ma J, Xu M, Xia T, et al. Silver nanoclusters show advantages in macrophage tracing *in vivo* and modulation of anti-tumor immuno-microenvironment. J Control Release. 2022;348:470–82.
26. Zhang C, Bu WB, Ni DL, Zhang SJ, Li Q, Yao ZW, et al. Synthesis of iron nanometallic glasses and their application in cancer therapy by a localized Fenton reaction. Angew Chem Int Edit. 2016;55(6):2101–6.
27. Chen J, Xia Y, Lan Q, Hu M, Xu YY, Wu QX, et al. Alginate based photothermal cryogels boost ferrous-supply for enhanced antibacterial chemodynamic therapy and accelerated wound healing. Int J Biol Macromol. 2023;232:23473.
28. Wang RH, Liu QW, Gao A, Tang N, Zhang Q, Zhang AM, et al. Recent developments of sonodynamic therapy in antibacterial application. Nanoscale. 2022;14(36):12999–3017.
29. Feng XB, Ma L, Lei J, Ouyang QL, Zeng YX, Luo Y, et al. Piezo-augmented Sonosensitizer with strong ultrasound-propelling ability for efficient treatment of osteomyelitis. ACS Nano. 2022;16(2):2546–57.
30. Kolarikova M, Hosikova B, Dilenko H, Barton-Tomankova K, Valkova L, Bajgar R, et al. Photodynamic therapy: innovative approaches for antibacterial and anticancer treatments. Med Res Rev. 2023;43(4):717–74.
31. Chen Y, Gao YJ, Chen Y, Liu L, Mo AC, Peng Q. Nanomaterials-based photothermal therapy and its potentials in antibacterial treatment. J Control Release. 2020;328:251–62.
32. Li J, Liu XM, Tan L, Cui ZD, Yang XJ, Liang YQ, et al. Zinc-doped prussian blue enhances photothermal clearance of *Staphylococcus aureus* and promotes tissue repair in infected wounds. Nat Commun. 2019;10:4490.
33. Huo J, Jia Q, Huang H, Zhang J, Li P, Dong X, et al. Emerging photothermal-derived multimodal synergistic therapy in combating bacterial infections. Chem Soc Rev. 2021;50(15):8762–89.
34. Zhao Q, Wang J, Yin C, Zhang P, Zhang J, Shi M, et al. Near-Infrared Light-Sensitive Nano Neuro-Immune Blocker Capsule relieves Pain and enhances the Innate Immune response for necrotizing infection. Nano Lett. 2019;19(9):5904–14.
35. Pallavicini P, Bassi B, Chirico G, Collini M, Dacarro G, Fratini E, et al. Modular approach for bimodal antibacterial surfaces combining photo-switchable activity and sustained biocidal release. Sci Rep. 2017;7(1):5259.
36. Fan X, Yang F, Nie C, Yang Y, Ji H, He C, Cheng C, Zhao C. Mussel-inspired synthesis of NIR-Responsive and Biocompatible Ag-Graphene 2D nanoagents for versatile bacterial disinfections. ACS Appl Mater Interfaces. 2018;10(1):296–307.
37. Masters EA, Ricciardi BF, Bentley KLM, Moriarty TF, Schwarz EM, Muthukrishnan G. Skeletal infections: microbial pathogenesis, immunity and clinical management. Nat Rev Microbiol. 2022;20(7):385–400.
38. Seebach E, Kubatzky KF. Chronic Implant-related bone infections-can immune modulation be a therapeutic strategy? Front Immunol. 2019;10:1724.
39. Yamada KJ, Heim CE, Xi X, Attri KS, Wang D, Zhang W, et al. Monocyte metabolic reprogramming promotes pro-inflammatory activity and *Staphylococcus aureus* biofilm clearance. PLoS Pathog. 2020;16(3):e1008354.
40. Brandt SL, Klopfenstein N, Wang S, Winfree S, McCarthy BP, Territo PR, et al. Macrophage-derived LTB4 promotes abscess formation and clearance of *Staphylococcus aureus* skin infection in mice. PLoS Pathog. 2018;14(8):e1007244.
41. Yu YJ, Yan JH, Chen QW, Qiao JY, Peng SY, Cheng H, et al. Polymeric nanosystem for macrophage reprogramming and intracellular MRSA eradication. J Control Release. 2023;353:591–610.
42. Park MD, Silvin A, Ginhoux F, Merad M. Macrophages in health and disease. Cell. 2022;185(23):4259–79.
43. Cheng YJ, Zhang YF, Zhao Z, Li G, Li J, Li AR, et al. Guanidinium-decorated nanostructure for precision sonodynamic-catalytic therapy of MRSA-infected osteomyelitis. Adv Mater. 2022;34(50):e2206646.
44. Zhou YF, Fan SY, Feng LL, Huang XL, Chen XY. Manipulating intratumoral Fenton chemistry for enhanced chemodynamic and chemodynamic-synergized multimodal therapy. Adv Mater. 2021;33(48):e2104223.
45. Tang ZM, Liu YY, He MY, Bu WB. Chemodynamic therapy: Tumour microenvironment-mediated Fenton and Fenton-like reactions. Angew Chem Int Edit. 2019;58(4):946–56.
46. Wang HB, Wang MJ, Xu XH, Gao P, Xu ZL, Zhang Q, et al. Multi-target mode of action of silver against *Staphylococcus aureus* endows it with capability to combat antibiotic resistance. Nat Commun. 2021;12(1):3331.
47. Buzzo JR, Devaraj A, Gloag ES, Jurcisek JA, Robledo-Avila F, Kesler T, et al. Z-form extracellular DNA is a structural component of the bacterial biofilm matrix. Cell. 2021;184(23):5740–58.
48. Li YQ, Xiu WJ, Yang KL, Wen QR, Yuwen LH, Luo ZC, et al. A multifunctional Fenton nanoagent for microenvironment-selective anti-biofilm and anti-inflammatory therapy. Mater Horiz. 2021;8(4):1264–71.
49. Guo GY, Zhang HL, Shen H, Zhu CZ, He RK, Tang J, et al. Space-selective chemodynamic therapy of $CuFe_5O_8$ nanocubes for implant-related infections. ACS Nano. 2020;14(10):13391–405.
50. Gauthier T, Chen WJ. Modulation of macrophage immunometabolism: a new approach to fight infections. Front Immunol. 2022;13:780839.
51. Russell DG, Huang L, VanderVen BC. Immunometabolism at the interface between macrophages and pathogens. Nat Rev Immunol. 2019;19(5):291–304.
52. Shi L, Luo M, Chen WR, Hu C, Zhang GL, Zhang FH, et al. In situ photoimmunotherapy for cutaneous granuloma caused by itraconazole-resistant *Candida guilliermondii*. Dermatol Ther. 2016;29(5):353–7.
53. Zhang C, Hu DF, Xu JW, Ma MQ, Xing HB, Yao K, et al. Polyphenol-assisted exfoliation of transition metal dichalcogenides into nanosheets as photothermal nanocarriers for enhanced antibiofilm activity. ACS Nano. 2018;12(12):12347–56.
54. Huang M, Ye K, Hu T, Liu K, You M, Wang L, et al. Silver nanoparticles attenuate the antimicrobial activity of the Innate Immune System by inhibiting neutrophil-mediated phagocytosis and reactive oxygen species production. Int J Nanomed. 2021;16:1345–60.
55. Wang S, Chen Y, Ling Z, Li J, Hu J, He F, et al. The role of dendritic cells in the immunomodulation to implanted biomaterials. Int J Oral Sci. 2022;14(1):52.
56. Zhang ST, Qu XH, Jiao JY, Tang HZ, Wang MQ, Wang Y, et al. Felodipine enhances aminoglycosides efficacy against implant infections caused by methicillin-resistant *Staphylococcus aureus*, persisters and biofilms. Bioact Mater. 2022;14:272–89.

57. Yuan Z, Lin CC, He Y, Tao BL, Chen MW, Zhang JX, et al. Near-infrared light-triggered nitric-oxide-enhanced photodynamic therapy and low-temperature photothermal therapy for biofilm elimination. ACS Nano. 2020;14(3):3546–62.
58. Lyu ZC, Zhao YC, Huo SC, Wang F, Meng XC, Yuan ZG, et al. Mussel-inspired dopamine-Cu-II coated polyetheretherketone surface with direct and immunomodulatory effect to facilitate osteogenesis, angiogenesis, and antibacterial ability. Mater Des. 2022;222:111069.
59. Malachowa N, Kobayashi SD, Lovaglio J, DeLeo FR. Mouse model of Staphylococcus aureus skin infection. Methods Mol Biol. 2019;1960:139–47.

Publisher's Note